

AIAA-81-0112

**A Third-Order-Accurate Upwind
Scheme for Navier-Stokes
Solutions at High Reynolds Numbers**

R.K. Agarwal, McDonnell Douglas
Research Labs, St. Louis, Mo.

**AIAA 19th
AEROSPACE SCIENCES MEETING**

January 12-15, 1981/St. Louis, Missouri

A THIRD-ORDER-ACCURATE UPWIND SCHEME FOR NAVIER-STOKES SOLUTIONS AT HIGH REYNOLDS NUMBERS*

R. K. Agarwal**

McDonnell Douglas Corporation
St. Louis, Missouri 63166

Abstract

A third-order-accurate upwind scheme is presented for solution of the steady 2-D Navier-Stokes equations in stream-function/vorticity form. The scheme is found to be accurate and stable at high Reynolds numbers. A series of test computations is performed on flows with large recirculating regions. In particular, highly accurate solutions are obtained for flow in a driven square cavity (which has become a standard test case for evaluating the accuracy, stability, and efficiency of Navier-Stokes algorithms) up to Reynolds numbers of 10^4 . These computations are used to critically evaluate the accuracy of other existing first- and second-order-accurate upwind schemes. In addition, computations are carried out for flow in a channel with symmetric sudden expansion, flow in a channel with a symmetrically placed blunt base, and the flowfield of an impinging jet. Good agreement is obtained with the computations of other investigators as well as with the available experimental data.

Nomenclature

h	mesh size
H	base half-width or the inverse of the expansion-ratio for a channel with sudden expansion
H_j	height of the jet above the ground plane
(i, j)	mesh coordinates
ℓ	reattachment length
ℓ_c	eddy-center distance in the x-direction from the origin
r_ψ	root-mean-square residual norm for ψ
r_ω	root-mean-square residual norm for ω
Re	Reynolds number ($U_{av} \cdot l/\nu$)
Re_H	Reynolds number ($U_{av} \cdot H/\nu$)
Re_j	Reynolds number ($V_{max} \cdot H_j/\nu$)
(u, v)	velocity components in (x, y) directions
U_{av}	average velocity at the inflow boundary
V_{max}	maximum velocity of the impinging jet
(x, y)	cartesian coordinates
ϕ	transport property of the fluid (ψ or ω)
ψ	stream function
ω	vorticity

Subscripts:

p	values at the plate
c	values at the eddy-center

Introduction

It is well known that an upwind bias is necessary in differencing the convection terms in the steady-state Navier-Stokes equations for obtaining stable solutions at high Reynolds numbers. The standard central differencing of the convection terms destroys the elliptic nature of the difference equations at high Reynolds numbers because of loss of diagonal dominance in the resulting matrix. The majority of the solution algorithms for the steady Navier-Stokes equations employ first-order-accurate upwind differencing¹ or a hybrid of first-order upwind and central-differencing.² In a first-order upwind scheme, if u is the convection velocity in the x direction, the first-order derivative in the convection terms written at a mesh point i is:

$$u \left(\frac{\partial \phi}{\partial x} \right)_i = u \left[\frac{\phi_i - \phi_{i-1}}{\Delta x} \right] \text{ if } u > 0 \quad (1a)$$

and

$$u \left(\frac{\partial \phi}{\partial x} \right)_i = u \left[\frac{\phi_{i+1} - \phi_i}{\Delta x} \right] \text{ if } u < 0, \quad (1b)$$

where ϕ is a transport property of the fluid. The main criticism of employing the difference operators [Eq. (1)] is the introduction of a large artificial diffusion in the direction of the bias, thereby resulting in a considerable loss of accuracy. Furthermore, while the central-differenced diffusion operator in the Navier-Stokes equations is third-order accurate, the convection operator is only first-order accurate, resulting in the overall accuracy of the algorithm being first-order in mesh size. Atias, Wolfshtein, and Israeli³ have proposed a second-order-accurate upwind scheme, which is written

$$u \left(\frac{\partial \phi}{\partial x} \right)_i = u \left[\frac{-3\phi_i + 4\phi_{i+1} - \phi_{i+2}}{2\Delta x} \right] \text{ if } u < 0 \quad (2a)$$

and

$$u \left(\frac{\partial \phi}{\partial x} \right)_i = u \left[\frac{3\phi_i - 4\phi_{i-1} + \phi_{i-2}}{2\Delta x} \right] \text{ if } u > 0. \quad (2b)$$

Although this scheme has not been tested as extensively as the first-order-accurate scheme, the relative accuracy of the convection operator is an order less than that of the diffusion operator. Furthermore, the scheme tends to exhibit instability at high Reynolds numbers. On the basis of a von Neumann type stability analysis for the linearized equations, Atias, Wolfshtein, and Israeli³ find that a Gauss-Seidel solution of the second-order upwind scheme is stable if the mesh Reynolds number is less than $2 + \sqrt{8}$ (this value is 2 for a central-difference scheme).

A third-order-accurate upwind scheme is proposed in this paper. In this scheme, both the convection and diffusion operators are third-order accurate. The resulting matrix remains diagonally dominant at all Reynolds numbers.

*This research was conducted under McDonnell Douglas Independent Research and Development Program.

**Research Scientist, McDonnell Douglas Research Laboratories; Member AIAA.

The first-order derivative at a mesh point "i" can be written, using a Taylor series expansion, as

$$\left. \frac{\partial \phi}{\partial x} \right|_i = \frac{\phi_{i+1} - \phi_i}{\Delta x} - \frac{(\Delta x)^2}{6} \left. \frac{\partial^3 \phi}{\partial x^3} \right|_i + \dots$$

Now if $u > 0$, we write

$$\begin{aligned} \left. \frac{\partial^3 \phi}{\partial x^3} \right|_i &= \frac{\left. \frac{\partial^2 \phi}{\partial x^2} \right|_{i+1} - \left. \frac{\partial^2 \phi}{\partial x^2} \right|_i}{\Delta x} \\ &= \frac{(\phi_{i+1} - 2\phi_i + \phi_{i-1}) - (\phi_{i-2} - 2\phi_{i-1} + \phi_i)}{(\Delta x)^3} \\ &= \frac{\phi_{i+1} - 3\phi_i + 3\phi_{i-1} - \phi_{i-2}}{(\Delta x)^3} \end{aligned}$$

If $u < 0$,

$$\begin{aligned} \left. \frac{\partial^3 \phi}{\partial x^3} \right|_i &= \frac{\left. \frac{\partial^2 \phi}{\partial x^2} \right|_{i+1} - \left. \frac{\partial^2 \phi}{\partial x^2} \right|_i}{\Delta x} \\ &= \frac{(\phi_{i+2} - 2\phi_{i+1} + \phi_i) - (\phi_{i+1} - 2\phi_i + \phi_{i-1})}{(\Delta x)^3} \\ &= \frac{\phi_{i+2} - 3\phi_{i+1} + 3\phi_i - \phi_{i-1}}{(\Delta x)^3} \end{aligned}$$

The difference operators for the first-order derivatives in the convection terms thus become

$$u \left(\frac{\partial \phi}{\partial x} \right)_i = -u \left[\frac{2\phi_{i+1} + 3\phi_i - 6\phi_{i-1} + \phi_{i-2}}{6\Delta x} \right] \text{ if } u > 0 \quad (3a)$$

and

$$-u \left(\frac{\partial \phi}{\partial x} \right)_i = -u \left[\frac{\phi_{i+2} + 6\phi_{i+1} - 3\phi_i - 2\phi_{i-1}}{6\Delta x} \right] \text{ if } u < 0. \quad (3b)$$

The Difference Equations

The steady Navier-Stokes equations in the stream-function/vorticity form are

$$\nabla^2 \psi = \omega \quad (4a)$$

$$\nabla^2 \omega + \text{Re} \left(\frac{\partial \psi}{\partial x} \frac{\partial \omega}{\partial y} - \frac{\partial \psi}{\partial y} \frac{\partial \omega}{\partial x} \right) = 0, \quad (4b)$$

where ψ denotes the stream function and ω the vorticity. The Poisson equation for the stream function is discretized using central differences, while the vorticity equation is discretized using the third-order upwind scheme. The difference equations on a uniform mesh of spacing h at a mesh point (i, j) can be written as

$$\psi_{i+1,j} + \psi_{i-1,j} + \psi_{i,j+1} + \psi_{i,j-1} - 4\psi_{i,j} = \omega_{i,j} h^2 \quad (5)$$

and

$$\begin{aligned} &\Lambda_1(i, j) \omega_{i+2,j} + \Lambda_2(i, j) \omega_{i+1,j} + \Lambda_3(i, j) \omega_{i,j} \\ &+ \Lambda_4(i, j) \omega_{i-1,j} + \Lambda_5(i, j) \omega_{i-2,j} + \Lambda_6(i, j) \omega_{i,j-1} \\ &+ \Lambda_7(i, j) \omega_{i,j-2} + \Lambda_8(i, j) \omega_{i,j+1} + \Lambda_9(i, j) \omega_{i,j+2} = 0, \end{aligned} \quad (6)$$

where

$$\begin{aligned} \Lambda_1(i, j) &= \frac{\text{Re}}{24} [\beta_{ij} - |\beta_{ij}|], \\ \Lambda_2(i, j) &= 1 + \frac{\text{Re}}{6} [|\beta_{ij}| - 2\beta_{ij}], \\ \Lambda_3(i, j) &= -[4 + \frac{\text{Re}}{4} (|\alpha_{ij}| + |\beta_{ij}|)], \\ \Lambda_4(i, j) &= 1 + \frac{\text{Re}}{6} [2\beta_{ij} + |\beta_{ij}|], \\ \Lambda_5(i, j) &= -\frac{\text{Re}}{24} [\beta_{ij} + |\beta_{ij}|], \\ \Lambda_6(i, j) &= 1 + \frac{\text{Re}}{6} [|\alpha_{ij}| - 2\alpha_{ij}], \\ \Lambda_7(i, j) &= \frac{\text{Re}}{24} [\alpha_{ij} - |\alpha_{ij}|], \\ \Lambda_8(i, j) &= 1 + \frac{\text{Re}}{6} [|\alpha_{ij}| + 2\alpha_{ij}], \\ \Lambda_9(i, j) &= -\frac{\text{Re}}{24} [\alpha_{ij} + |\alpha_{ij}|], \end{aligned}$$

and

$$\alpha_{ij} = (\psi_{i+1,j} - \psi_{i-1,j}), \beta_{ij} = (\psi_{i,j+1} - \psi_{i,j-1}).$$

The difference equations [Eqs. (5) and (6)] are solved by an alternating direction-line iterative (ADI) algorithm.

Thomas's tridiagonal algorithm is used to solve Eq. (5), and Eq. (6) is solved using a penta-diagonal matrix inversion subroutine. For most of the computations, a relaxation factor of 1.2 for the stream-function equation [Eq. (5)] and 0.8 for the vorticity equation [Eq. (6)] were found to be optimum. However, the numerical experiments indicate that higher relaxation factors can be used at lower Reynolds numbers, but an under-relaxation of the vorticity equation becomes necessary for obtaining convergence at high Reynolds numbers. For each flow variable ψ and ω , root-mean-square residuals are defined as follows:

$$\begin{aligned} r_\psi &= \sqrt{\sum_{ij} \left[(\psi_{N+1} - \psi_N)_{ij} \right]^2} / h \\ r_\omega &= \sqrt{\sum_{ij} \left[(\omega_{N+1} - \omega_N)_{ij} \right]^2} / h, \end{aligned}$$

where N is the iteration counter. Convergence is considered to be achieved when r_ψ and r_ω are $< 10^{-4}$.

Boundary Conditions

There is considerable discussion in the literature³⁻⁵ on the influence of boundary approximations on the stability and accuracy of Navier-Stokes solutions in stream-function/vorticity form.

The four examples of flow considered in this paper cover most types of boundary conditions generally encountered in engineering applications. The boundary conditions for the stream function or its gradient are easily prescribed; the vorticity boundary condition, however, requires careful implementation.

The major difficulty lies in approximating the vorticity value at a no-slip boundary. There are first-order, second-order, and third-order-accurate difference formulae that approximate the vorticity at a no-slip boundary in terms of the stream function values in the interior. With reference to Fig. 1, these formulae can be written as

$$\omega_B = -\frac{2(\psi_{B+1} - \psi_B)}{h^2} + \frac{2}{h} \left(\frac{\partial \psi}{\partial y} \right)_B + O(h) \quad (7a)$$

$$\omega_B = -\frac{(8\psi_{B+1} - \psi_{B+2} - 7\psi_B)}{2h^2} + \frac{3}{h} \left(\frac{\partial \psi}{\partial y} \right)_B + O(h^2) \quad (7b)$$

$$\omega_B = -\frac{(21\psi_{B+1} - 6\psi_{B+2} + \psi_{B+3} - 16\psi_B)}{3h^2} + \frac{4}{h} \left(\frac{\partial \psi}{\partial y} \right)_B + O(h^2), \quad (7c)$$

where B, B+1, etc. denote points on the wall, one point in from the wall, etc.; $(\partial \psi / \partial y)_B$ is in general zero unless the wall is moving. For any other orientation of the solid surface, $(\partial \psi / \partial y)_B$ in Eqs. (7a) - (7c) is replaced by $\partial \psi / \partial n)_B$, where n denotes the outward normal to the no-slip wall.

Another frequently used formula attributed to Woods⁶ relates the vorticity at the solid boundary with vorticity at an interior field point adjacent to the boundary point in the normal direction:

$$\omega_B = \frac{3}{h^2} (\psi_{B+1} - \psi_B) - \frac{\omega_{B+1}}{2} + O(h^3). \quad (8)$$

There are many other higher-order-accurate formulae known as (p,q) formulae in their generalized form. These are

$$(\omega_B)_i = - \left[-2q^3 \alpha \psi_{i,p} + 2p^3 \alpha \psi_{i,q} + \psi_{i+1,B} + \psi_{i-1,B} - \frac{2(p+q)}{pq} h \left(\frac{\partial \psi}{\partial y} \right)_B - (2 + 2p^3 \alpha - 2q^3 \alpha) \psi_{i,B} \right] / h^2, \quad (9)$$

where p and q are positive integers, $p \neq q$, and $\alpha = p^{-2} q^{-2} (p - q)^{-1}$.

A discussion of these formulae is given in Ref. 4. The influence of all these boundary approximations for vorticity at a no-slip wall on the global accuracy and stability of the solution has been investigated by many researchers. However, no clear consensus has emerged, and often the conclusions of various investigations are conflicting. For steady Navier-Stokes equations, most of these boundary formulae have been tested in conjunction with a first-order-accurate upwind algorithm for the interior field points. Our experience indicates that if the numerical scheme is only first-order accurate, a higher-order accurate formula for vorticity at a no-slip boundary improves the solution only marginally; often it may cause serious convergence problems, particularly at high Reynolds numbers, if the initial guess is not sufficiently close to the actual solution.

On the other hand, if the numerical scheme is of higher-order accuracy, e.g., the present third-order accurate scheme, a lower-order-accurate formula for ω_B does not significantly deteriorate the accuracy of the overall global solution on a reasonable mesh.

This conclusion is also borne out by the computations of Benjamin and Denny⁷ for cavity flow at high Reynolds numbers (of the order 10^4) using a central-difference algorithm based on the unsteady Navier-Stokes equations. In our computations, we have tested all three boundary vorticity formulae [Eqs. (7a) - (7c)] in conjunction with the third-order accurate scheme. A converged solution at a given Reynolds number is first obtained using a first-order-accurate boundary formula. This solution is then used as an initial guess to obtain a converged solution using a second-order-accurate boundary formula and so on. Each step takes only a few extra iterations. This step-wise procedure avoids the stability problems introduced by using a higher-order-accurate boundary formula from the outset.

There is an additional aspect of the boundary conditions specific to the third-order-accurate algorithm for the vorticity equation. The solution of Eq. (6) at an interior grid point next to the physical boundaries of the flowfield requires specification of the vorticity value outside the physical domain (at points A-1, B-1, D+1, E+1, etc. in Fig. 1). This specification poses no difficulty at the inflow or outflow boundaries or in the symmetry plane because usually the gradient $(\partial \omega / \partial n)$ or the second-order derivative $(\partial^2 \omega / \partial n^2)$ may be specified. The solution of Eq. (6) at an interior grid point next to the solid wall (point B+1 in Fig. 1), however, requires specification of the vorticity value at a grid point exterior to the physical domain (point B-1 in Fig. 1). This value is obtained by quadratic extrapolation of vorticity at the exterior point B-1 from the known values at the three consecutive interior values in the normal direction inside the physical domain. The vorticity ω_{B-1} is given by

$$\omega_{B-1} = 3\omega_B - 3\omega_{B+1} + \omega_{B+2}. \quad (10)$$

In general, at all such boundaries where the gradient $(\partial \omega / \partial n)$ or second-order derivative $(\partial^2 \omega / \partial n^2)$ is not specified, a quadratic extrapolation can be used to prescribe the vorticity at a grid point adjacent but exterior to the physical domain of the flow. Quadratic extrapolation has also been used by Leonard⁸ in his third-order-accurate QUICK algorithm for the 1-D convection-diffusion equation. An alternative to specifying vorticity at the point B-1 in Fig. 1 by quadratic extrapolation is to compute the value of vorticity at the dashed line in Fig. 1 using Eq. (5) and then solve Eq. (6) for the interior points B+2, B+3, etc. The computation of ω_{B+1} using Eq. (5) requires computation of ψ values at the dashed line from the boundary condition $(\partial \psi / \partial n)_B = 0$ at a no-slip wall. Using one-sided differences $(\partial \psi / \partial n)_B = 0$ implies

$$\psi_{i,B+1} = (3\psi_{i,B} + \psi_{i,B+2})/4. \quad (11)$$

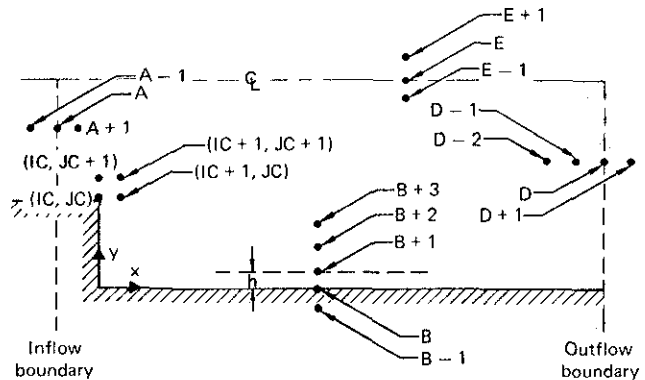


Fig. 1 Definition sketch for deriving boundary-value formulae in section 3.

The iterative solution cycle then goes through the following steps:

- construct initial distribution for ψ and ω ,
- advance ψ -equation one cycle,
- compute ψ_{B+1} at the dashed line in Fig. 1 using Eq. (11),
- compute ω_B from Eqs. (7a), (7b), or (7c) and ω_{B+1} from Eq. (5),
- advance ω -equation one cycle,
- determine root-mean-square residuals r_ψ and r_ω and test for convergence, and
- repeat steps (b) - (f) until convergence is achieved.

If quadratic extrapolation is used for the point B-1 in Fig. 1, the steps (c) and (d) change as follows:

- compute ω_B from Eq. (7a), (7b), or (7c), and
- compute ω_{B-1} from Eq. (10).

There are other salient aspects of the boundary conditions which are explained with the help of Fig. 1.

Boundary condition at the inflow boundary - Usually the inflow velocity profile is specified from which the stream-function and vorticity values at the inflow boundary can be calculated. Referring to Fig. 1, the vorticity at the point A-1 can be calculated using the quadratic interpolation formula [Eq. (10)] or using the equation recommended by Roache⁽⁹⁾ as well as Mueller and O'Leary:¹⁰

$$\left. \frac{\partial^2 \psi}{\partial x^2} \right|_A = 0. \quad (12)$$

Since $\omega = \partial v / \partial x - \partial u / \partial y$ and at the inflow boundary $u = U(y)$, Eq. (12) implies

$$\frac{\partial \omega}{\partial x} = 0$$

or

$$\omega_{A-1} = \omega_{A+1}.$$

Boundary condition at the centerline - At the centerline of the channel or the jet, $\psi = \omega = 0$. The specialization of the vorticity Eq. (4b) at the centerline gives an additional equation,

$$\frac{\partial^2 \omega}{\partial n^2} = 0, \quad (13)$$

where n is normal to the centerline. Eq. (13) gives

$$\omega_{E+1} = 2\omega_E - \omega_{E-1}.$$

Boundary condition at the outflow boundary - Downstream continuation is carried out using quadratic extrapolation formula similar to Eq. (10) for ψ as well as ω at the outflow boundary point D and an exterior point D+1.

Linear extrapolation formulae suggested by Mueller and O'Leary,¹⁰

$$\psi_D = 2\psi_{D-1} - \psi_{D-2} \quad (14a)$$

$$\omega_D = 2\omega_{D-1} - \omega_{D-2}, \quad (14b)$$

or those suggested by Hung and Macagno,¹¹

$$\psi_D = \psi_{D-4} - 2\psi_{D-3} + 2\psi_{D-1} \quad (14c)$$

$$\omega_D = \omega_{D-4} - 2\omega_{D-3} + 2\omega_{D-1}, \quad (14d)$$

can also be used without any significant change in the solution.

Vorticity at the corner - Again referring to Fig. 1, the vorticity at the corner C can be defined using Eq. (7a) in two ways:

$$(\omega_C)_I = 2(\psi_{IC,JC+1} - \psi_{IC,JC})/h^2 \quad (15a)$$

$$(\omega_C)_{II} = 2(\psi_{IC+1,JC} - \psi_{IC,JC})/h^2, \quad (15b)$$

When the vorticity at (IC,JC+1) is being evaluated, $(\omega_C)_I$ is used. When the vorticity at (IC+1,JC) is calculated, $(\omega_C)_{II}$ is used. As $h \rightarrow 0$, the limit of the sharp corner is thus retained.

Using Eq. (7b) or (7c), higher-order formulae for $(\omega_C)_I$ and $(\omega_C)_{II}$ can be obtained.

Computed Flowfields

All the computations reported in this paper have been carried out on a uniform mesh. Convergence of the solution was considered to be achieved when r_ψ and r_ω were $< 10^{-4}$. The solutions were obtained at a sequence of Reynolds numbers for each flow example. The converged solution at the lower Reynolds number was used as a starting initial guess for obtaining the solution at higher Reynolds number. First solutions in each case were obtained using the lowest-order boundary formula [Eq. (7a)] for the vorticity. Subsequent solutions employed the higher-order-accurate boundary-vorticity formulae [Eqs. (7b) and (7c)]. All the results presented in this paper are based on the third-order-accurate formulae for different types of boundary conditions discussed earlier. Mass flow was computed at the inflow and outflow boundaries, and its balance was checked in all computations.

Flow in a Driven Square Cavity

Usually, flow in a driven cavity is used as a standard test case for evaluating the stability and accuracy of Navier-Stokes algorithms. Figure 2 shows the geometry and the boundary conditions for this flow.

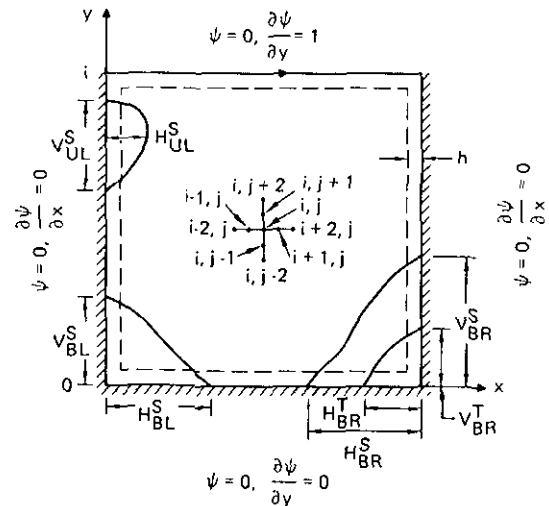


Fig. 2 Flow in a square-driven cavity - nomenclature and boundary conditions.

Most numerical schemes used to compute this flow give results in agreement with the rigorous calculations of Burggraf¹² for Reynolds numbers ≤ 400 . However, there is considerable disagreement in the calculations of various investigators for Reynolds numbers > 500 . The conflict occurs for $Re > 500$ for the bottom upstream-secondary-vortex and for $Re > 4000$

for the bottom downstream-secondary-vortex. Furthermore, the question whether the secondary vortices at the corner persist at still higher Reynolds numbers remains controversial. Nallasamy and Prasad,¹ who employed a first-order-accurate upwind scheme to compute the flow up to a Reynolds number of 10^4 , predict the disappearance of the corner eddies at $Re > 10^4$. Figure 3 shows the variation of secondary vortex sizes as a function of Reynolds numbers in their computation. Their results have been criticized by Rubin and Khosla¹³ and Benjamin and Denny,⁷ among others; there is considerable loss in accuracy at high Reynolds numbers because of large artificial diffusion in the numerical scheme introduced as a consequence of first-order-accurate upwind differencing of the convection terms. Recently, Benjamin and Denny⁷ have obtained highly accurate solutions using unsteady Navier-Stokes equations on a fine mesh for Reynolds numbers up to 10^4 . Their results indicate the persistence of secondary bottom-corner vortices for $Re > 10^4$ as shown in Fig. 3, contrary to Nallasamy and Prasad's¹ conclusions. In addition, they indicate the appearance of tertiary and higher-order vortices as the Reynolds number increases above 1000. Benjamin and Denny's⁷ results are the only studies reported that show such a trend in secondary vortex sizes with Reynolds number. The present computations confirm these trends as shown in Fig. 3. The present results also show the appearance of a tertiary vortex in the upstream bottom-corner at $Re = 7500$.

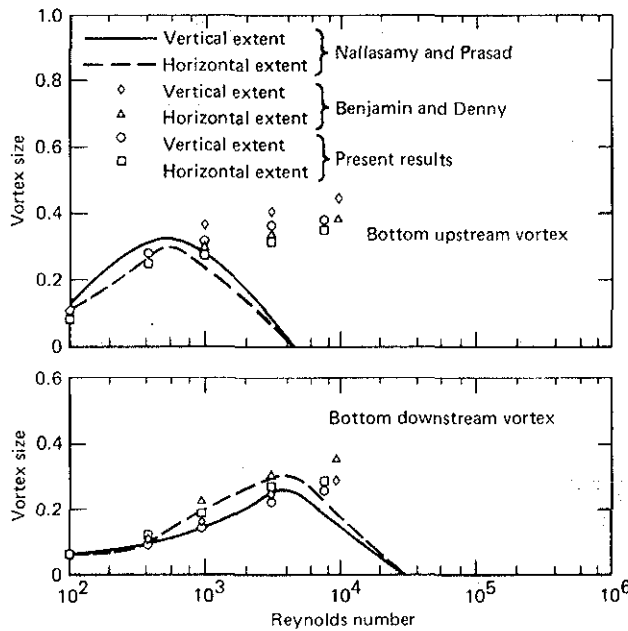


Fig. 3 Comparisons of secondary vortex sizes in a square-driven cavity as a function of Reynolds number.

Our computations also confirm an earlier inference by Mallinson and deVahl Davis¹⁴ wherein a secondary vortex in the upper upstream-corner is generated at a critical Reynolds number, estimated by Benjamin and Denny⁷ to be ~ 1200 . The present computations at $Re = 3200$ and 7500 indicate the presence of this secondary vortex in the upper upstream-corner of the cavity. Table 1 gives the secondary and tertiary vortex-sizes for various Reynolds numbers. Figure 2 defines the nomenclature for horizontal and vertical lengths of these secondary and tertiary vortices.

Also of interest are the trends in ψ and ω at the center of the main vortex. Table 2 gives the values of ψ and ω for various Reynolds numbers at the center of the primary vortex and the minimum and midpoint values of the vorticity at the moving plate. The present computations for these quantities are in excellent agreement with the results of Benjamin and Denny⁷ at all Reynolds numbers considered. At the center of the main vortex, ω has almost attained the asymptotic value -1.887 which is close to the analytical value (-1.886) calculated by Burggraf¹² in his application of Batchelor's model,¹⁵ consisting of an inviscid core with uniform vorticity coupled to boundary-layer flows at solid surfaces. At the center of the main vortex, ψ also has almost attained an asymptotic value 0.12 (estimated to be 0.1212 by Benjamin and Denny⁷).

Thus the present results are contrary to the idea that the secondary vortices disappear at high enough Re ; rather the results suggest that as $Re \rightarrow \infty$, the primary vortex becomes a centrally located, increasingly circular region of constant vorticity, essentially circumscribed by the boundaries of the cavity. A series of counter-rotating vortices occupies each of the lower corners, with the vertical and horizontal extents of the largest of these apparently approaching 0.5 . This picture of the flow structure in the stationary lower corners is in agreement with Moffatt's¹⁶ analytically derived model of an infinite series of rapidly diminishing counter-rotating vortices. Figures 4-8 show the development of flow structure in the cavity as the Reynolds number increases from 0 to 7500 .

To complete the documentation of the cavity flow, an often compared parameter of interest, the centerline velocity distribution at various Reynolds number, is presented in Figs. 9-11. Figure 9 shows the variation of centerline velocity distribution in the cavity for $Re = 0, 100$, and 400 . The results of present computations are in excellent agreement with those of Burggraf for $Re \leq 400$. Figure 10 shows the comparison of velocity profiles on vertical centerline of the cavity for $Re = 1000$, obtained with the first-order upwind scheme of Nallasamy and Prasad¹ and the strongly coupled implicit method of Rubin and Khosla,¹³ using the unsteady Navier-Stokes equations and the present third-order upwind scheme. Figure 11 presents centerline velocity profiles for Reynolds number of 3200 and 7500 .

Table 1 Secondary and tertiary vortex sizes at various Reynolds numbers for flow in a driven square cavity (Nomenclature used in this table is explained in Fig. 2.)

Re	Secondary vortex sizes									Tertiary vortex sizes		
	V_{BL}^S	H_{BL}^S	V_{BR}^S	H_{BR}^S	V_{UL}^S	H_{UL}^S	$(\psi_{BL})_{max}$	$(\psi_{BR})_{max}$	$(\psi_{UL})_{max}$	V_{BR}^T	H_{BR}^T	$(\psi_{BR})_{max}$
100	0.0339	0.0339	0.1023	0.0838	—	—	-0.513×10^{-7}	-0.741×10^{-5}	—	—	—	—
1000	0.1417	0.1489	0.2830	0.2742	—	—	-0.154×10^{-3}	-0.16×10^{-2}	—	—	—	—
3200	0.2279	0.2473	0.3630	0.3370	0.1666	0.0790	-0.975×10^{-3}	-0.276×10^{-2}	-0.52×10^{-3}	—	—	—
7500	0.2601	0.2655	0.3774	0.3695	0.2250	0.1270	-0.118×10^{-2}	-0.287×10^{-2}	-0.153×10^{-2}	0.0803	0.0670	0.942×10^{-5}

Table 2 Stream function and vorticity values at the primary vortex center at various Reynolds numbers for flow in a driven square cavity.

Re	Mesh size, h	Stream function at vortex center, ψ_c	Vorticity at vortex center, ω_c	Vorticity at mid point of moving plate, $(\omega_p)_{x=1/2}$	Minimum vorticity at the moving plate, $(\omega_p)_{\min}$
0	1/20	0.1000	3.0391	5.44	5.44
100	1/60	0.1032	3.1581	6.715	6.045
1000	1/60	0.1171	2.0676	14.01	12.31
3200	1/120	0.1199	1.9434	24.74	21.72
7500	1/120	0.1200	1.8877	34.15	30.10

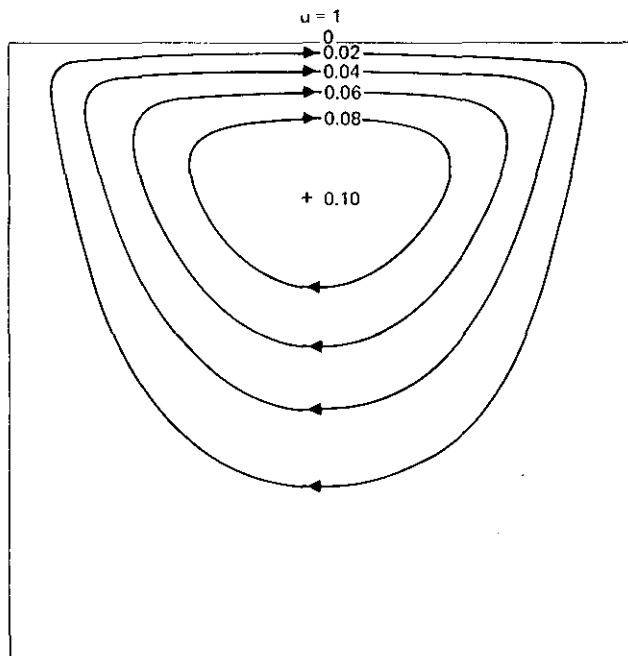


Fig. 4 Streamline-ψ contours at Re = 0 (21 x 21 grid).

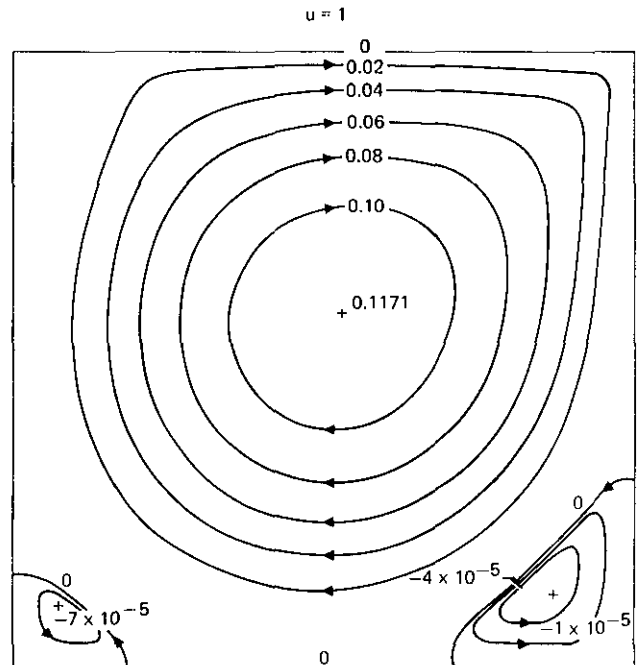


Fig. 6 Streamline-ψ contours at Re = 10³ (61 x 61 grid).

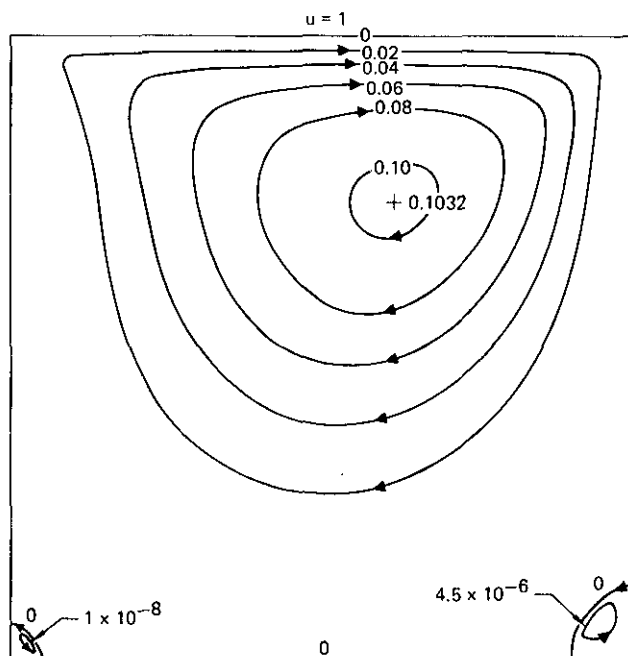


Fig. 5 Streamline-ψ contours at Re = 10² (61 x 61 grid).

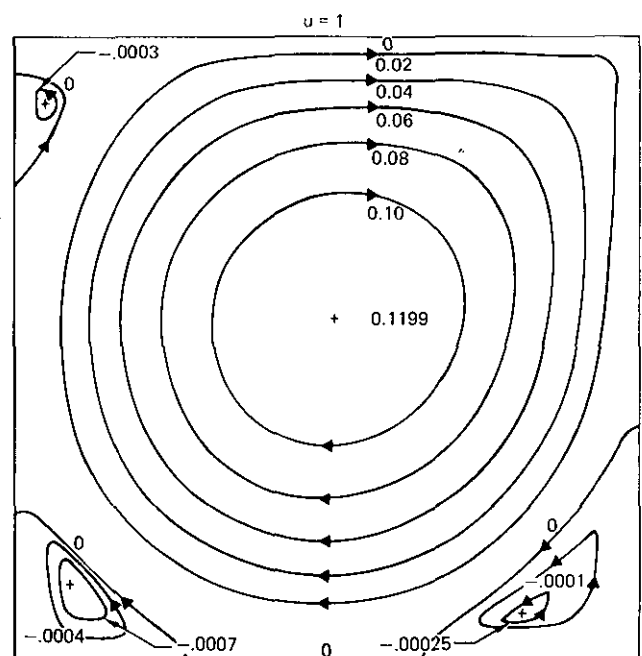


Fig. 7 Streamline-ψ contours at Re = 3.2 x 10³ (121 x 121 grid).

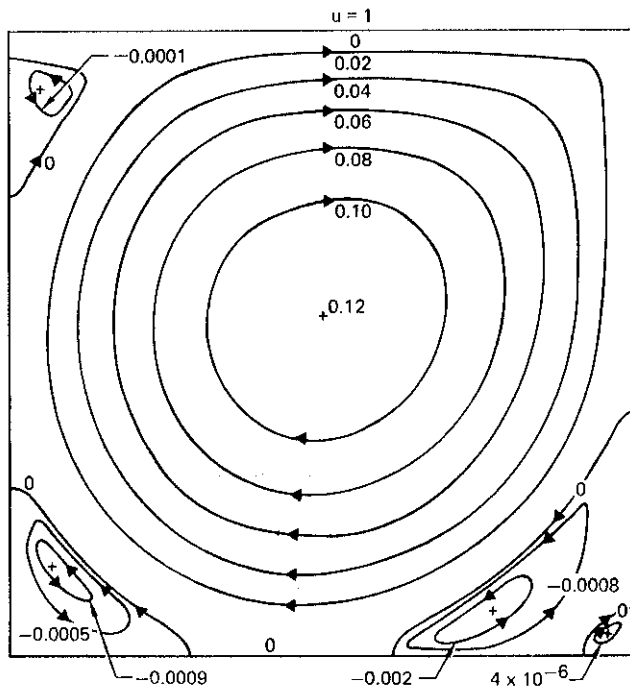


Fig. 8 Streamline- ψ contours at $Re = 7.5 \times 10^3$ (121 x 121 grid).

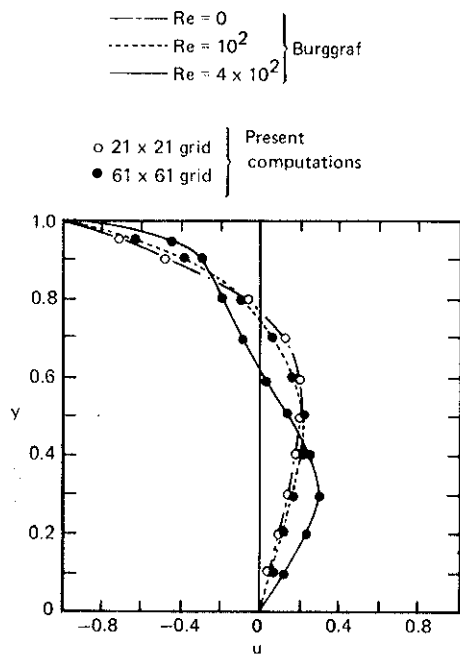


Fig. 9 Velocity profiles on vertical centerline of driven-square cavity at $Re = 0, 10^2$, and 4×10^2

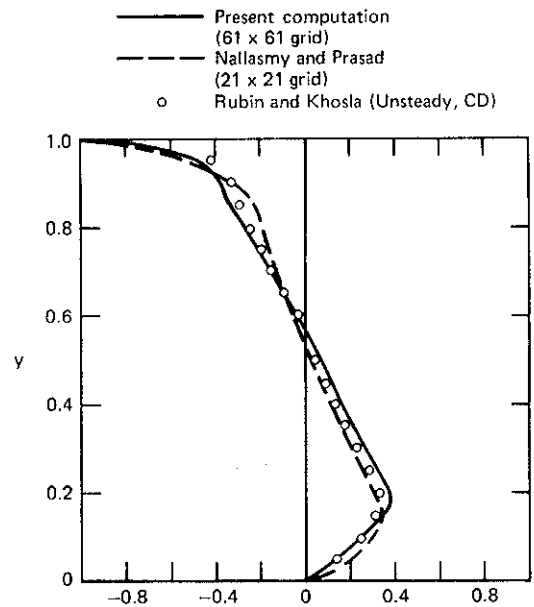


Fig. 10 Velocity profile on vertical centerline of driven-square cavity at $Re = 10^3$.

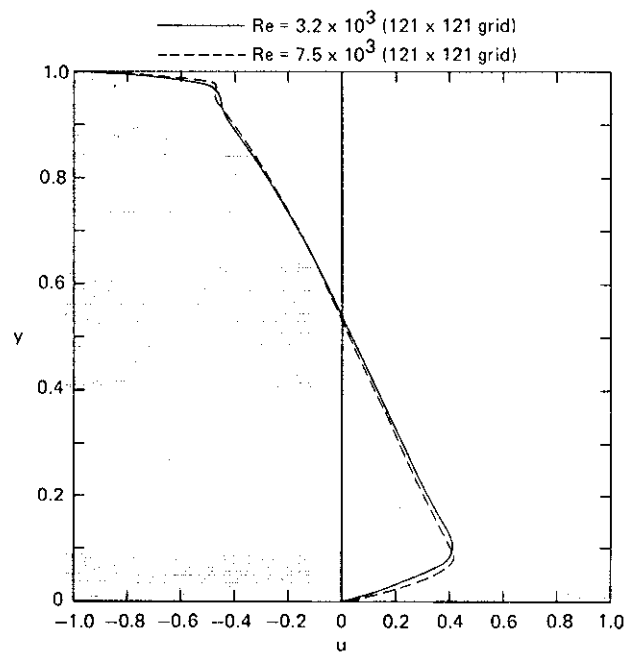


Fig. 11 Velocity profiles on vertical centerline of a driven-square cavity at $Re = 3.2 \times 10^3$ and 7.5×10^3 using the third-order upwind scheme.

Flow in a Channel with Sudden Symmetric Expansion

The geometry and boundary conditions for this flow are shown in Fig. 12. At the inflow boundary, a parabolic velocity profile was prescribed. For a given Reynolds number, the flow development length L was approximately estimated to define the axial extent of the computational domain. The Reynolds number for this configuration is based on the average velocity at the inflow boundary and the channel half-width downstream. Two sets of computations were carried out for which the computations and experimental results of other investigations are available for comparison.

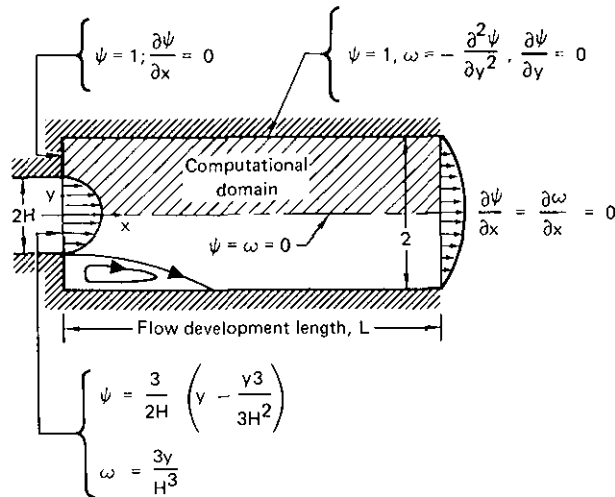


Fig. 12 Definition of the computational region for flow in a channel with symmetric sudden expansion.

The first set of computations was carried out for $Re = 46.6$ and the channel half-width at the inflow boundary $H = 0.5$. The streamwise length of the computational domain L was taken to be $24H$. A uniform mesh of grid spacing $h = 0.05$ was chosen. For this set of parameters, computations have been carried out by Hung and Macagno,¹¹ and Kumar and Yajnik.¹⁷ The present results are in excellent agreement with other computations as shown in Fig. 13. The reattachment length (ℓ), the location of the eddy center (ℓ_c), the stream function value at the eddy-center (ψ_e), and the minimum vorticity value (ψ_{pmin}) at the lower channel wall are all in excellent agreement with the computations of Hung and Macagno¹¹ and Kumar and Yajnik,¹⁷ the present results being perhaps more accurate. Figures 14 and 15 show the variation of streamwise velocity along the channel centerline and the distribution of vorticity at the upper wall of the channel respectively. Again the agreement between the present computations and those of Kumar and Yajnik¹⁷ is excellent. Figure 6 shows development of the streamwise velocity profile through the recirculating region to the fully developed flow.

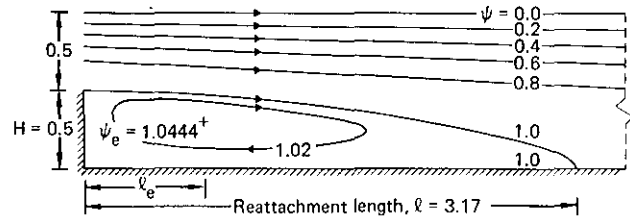


Fig. 13 Streamline- ψ contours for flow in a channel with symmetric sudden expansion, $Re = 46.6$, $H = 0.5$.

	ℓ/Re	ℓ_c/Re	$(\psi_e - 1)$	ω_{pmin}
Present computations	0.068	0.016	0.0444	-2.26
Hung and Macagno	0.066	0.013	0.052	-2.82
Kumar and Yajnik	0.064	0.014	0.045	-2.19

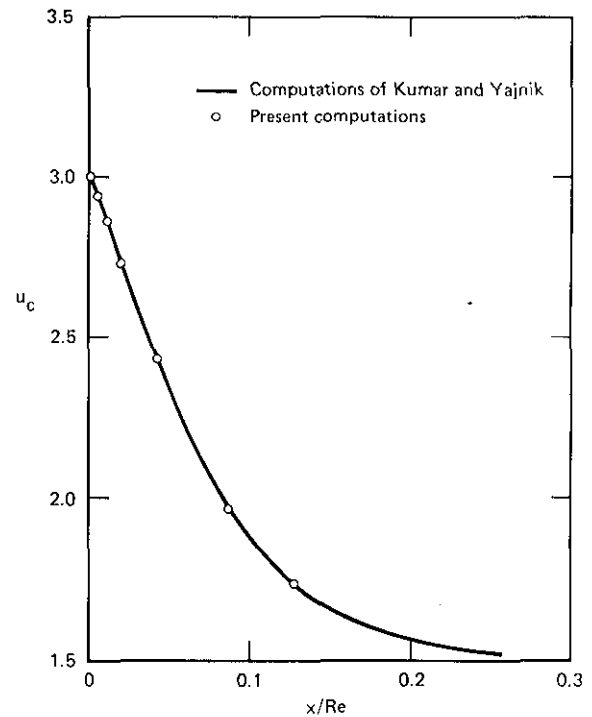


Fig. 14 Centerline velocity distribution for flow in a channel with a symmetric sudden expansion, $Re = 46.6$, $H = 0.5$.

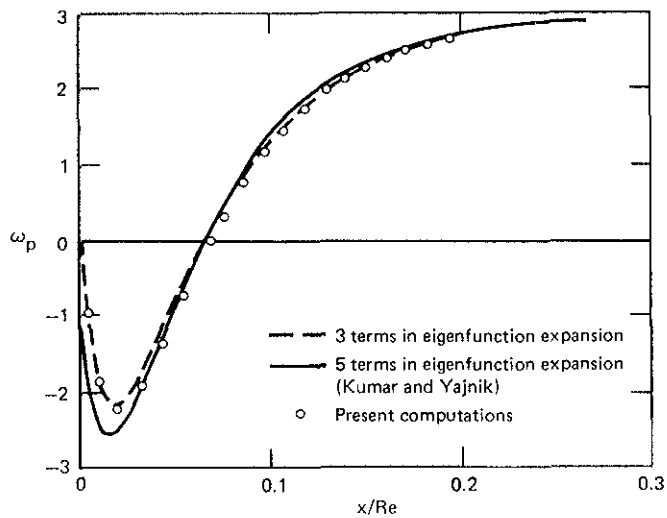


Fig. 15 Distribution of vorticity at the upper wall of the channel with symmetric sudden expansion, $Re = 46.6$, $H = 0.5$.

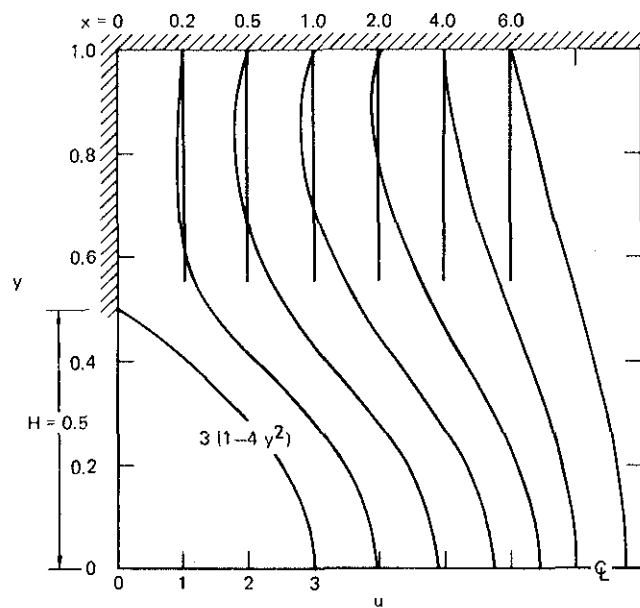


Fig. 16 Streamwise velocity profiles at various streamwise locations (x) for flow in a channel with sudden symmetric expansion, $Re = 46.6$, $H = 0.5$.

The second set of computations was carried out for $Re = 18.67$ and $H = 1/3$. These parameters correspond to the flow conditions in the experiment of Durst, Melling, and Whitelaw.¹⁸ For this case, the streamwise length of the computational domain L was taken to be $18H$ and the mesh spacing h was 0.05 . The computed value of the reattachment length ℓ compares well with the experimentally determined value as shown in Fig. 17. The other computed parameters, such as ℓ_e , ψ_e , and (ω_{pmin}) , could not be compared because of the unavailability of experimental information for these quantities. Figures 18 and 19 show the variation of streamwise velocity along the channel centerline and the distribution of vorticity at the upper wall of the channel respectively. Figure 20 shows the development of the streamwise velocity profile through the recirculating region to the fully

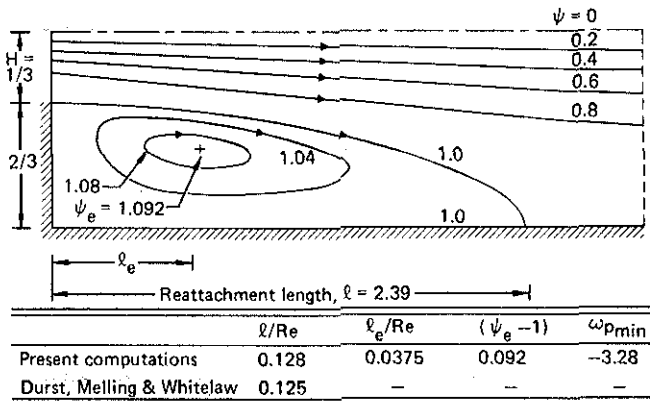


Fig. 17 Streamline- ψ contours for flow in a channel with symmetric sudden expansion, $Re = 18.67$, $H = 1/3$.

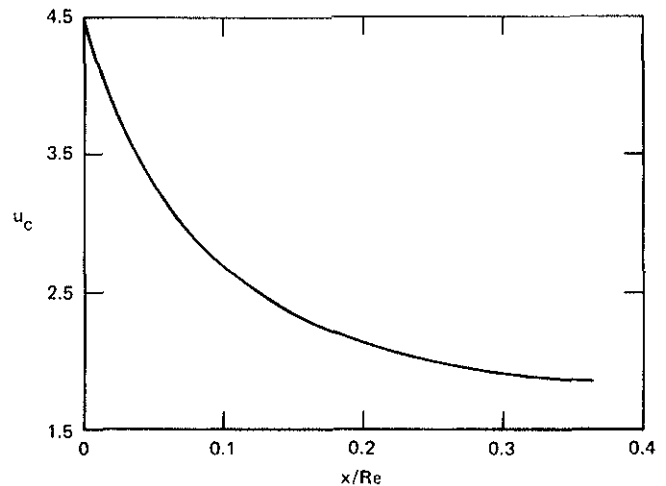


Fig. 18 Centerline velocity distribution for flow in a channel with a symmetric sudden expansion, $Re = 18.67$, $H = 1/3$.

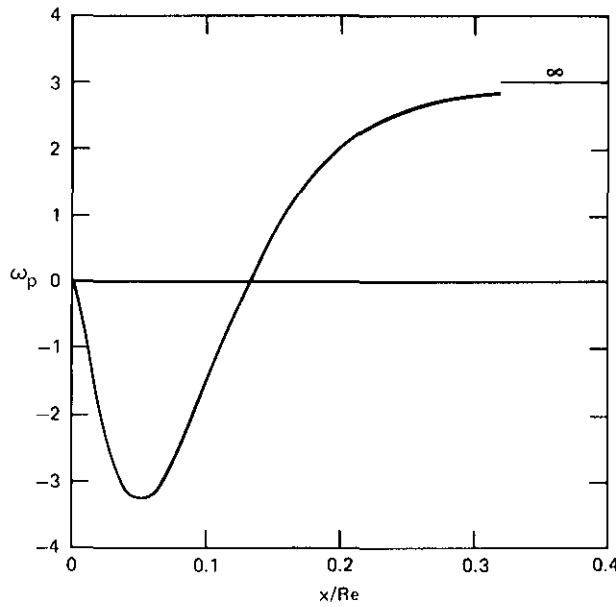


Fig. 19 Distribution of vorticity at the upper wall of the channel with symmetric sudden expansion, $Re = 18.67$, $H = 1/3$.

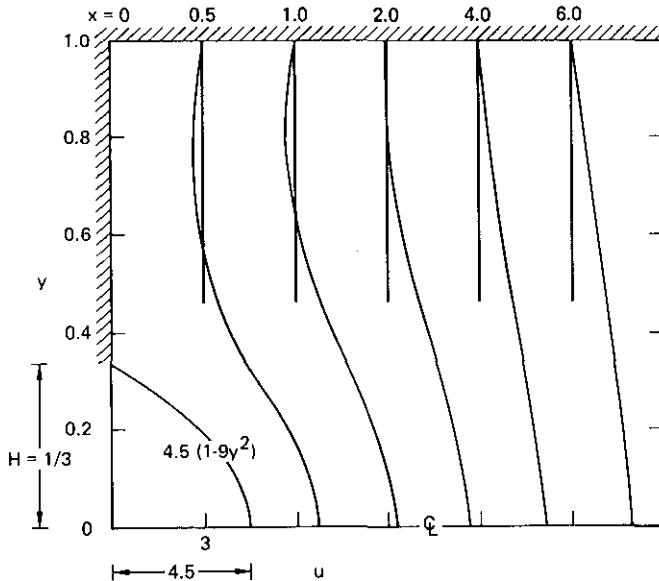


Fig. 20 Streamwise velocity profiles at various streamline locations (x) for flow in a channel with sudden symmetric expansion, $Re = 18.67$, $H = 1/3$.

developed flow. Figure 21 shows the effect of the expansion ratio $1/H$ on the reattachment length (ℓ/Re). The present computations are in excellent agreement with computations and experiments of other investigators.

Flow in a Channel with a Symmetrically Placed Blunt Base

The geometry and the boundary conditions for this flow are shown in Fig. 22. At the inflow boundary, a parabolic velocity profile is prescribed. For a given Reynolds number, the flow development length L was approximately estimated to define the axial extent of the computational domain. The Reynolds number for this configuration is based on the average velocity at the inflow boundary and the channel half-width downstream.

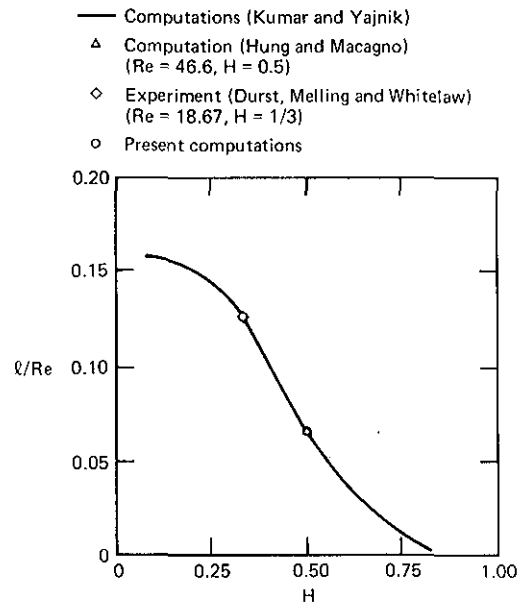


Fig. 21 The effect of expansion ratio ($1/H$) on the reattachment length (ℓ) for flow in a channel with a symmetric sudden expansion.

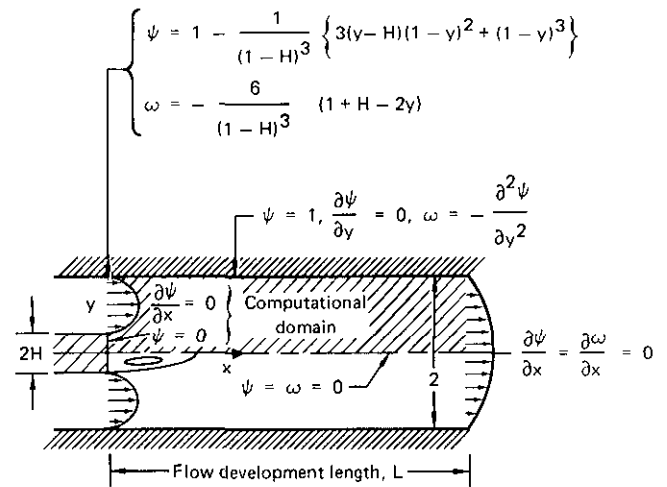


Fig. 22 Definition of the computational region for flow in a channel with a symmetrically placed blunt base.

Another Reynolds number Re_H (based on the average velocity and the base half-width) is also defined for comparison with the experimental results of Mueller and O'Leary.¹⁰ The two sets of computations for four different Reynolds numbers were carried out. In all these computations, L was taken to be six times the channel half-width downstream and the mesh size h was 0.05. Figure 23 shows the correlation between numerical and experimental results for eddy length ℓ and eddy-center location ℓ . The present computations compare well for the eddy length with the experimental values of Mueller and O'Leary.¹⁰ Computations of Mueller and O'Leary⁹ vary slightly from their experimental results for the eddy length. For the eddy-center location, the present computations and those of Mueller and O'Leary¹⁰ are in close agreement; the experimental values, however, are somewhat smaller in magnitude. This discrepancy can be attributed to the experimental uncertainty involved in exactly identifying the eddy center from the photographs.

Figure 23 also shows that the eddy size varies almost linearly with Reynolds number. This trend has been observed by various investigators theoretically as well as experimentally. 10,19,20

In Figs. 24-31 we provide documentation for two sets of flow parameters. In the first set, the flowfield is computed for a base half-width $H = 0.25$ at $Re = 30$ and 75 . Figure 24 shows the streamline contours, eddy length, and the eddy-center. Figures 25 and 26 show the variation of streamwise velocity along the channel centerline and the distribution of vorticity on the lower wall of the channel, respectively. Figure 27 shows the flow development through the recirculating region to the fully developed flow. In the second set the flowfield is computed for a base half-width $H = 0.5$ at $Re = 20$ and 50 . Figures 28-31 illustrate the streamline contours, vorticity distribution on the lower wall of the channel, streamwise velocity along the channel centerline, and the streamwise velocity profiles at various streamwise locations along the channel, respectively. In Figs. 24 and 28 separation occurs below the corner. A similar trend was found by Mueller and O'Leary.¹⁰

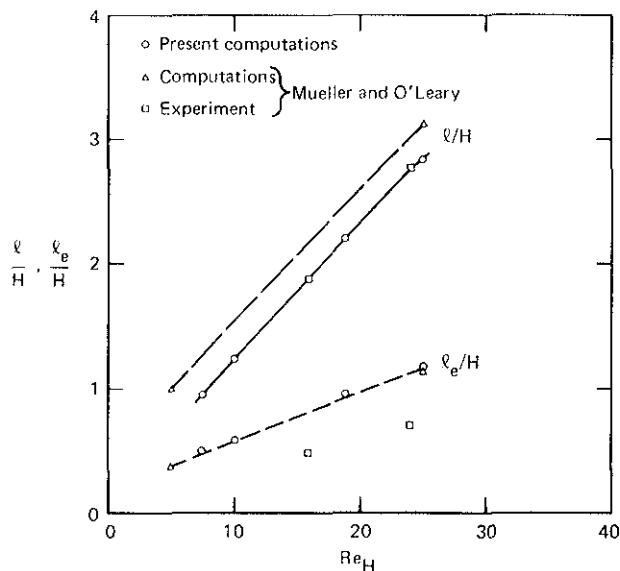


Fig. 23 Correlation of numerical and experimental results for eddy-length and eddy-center location for flow in a channel with a blunt base.

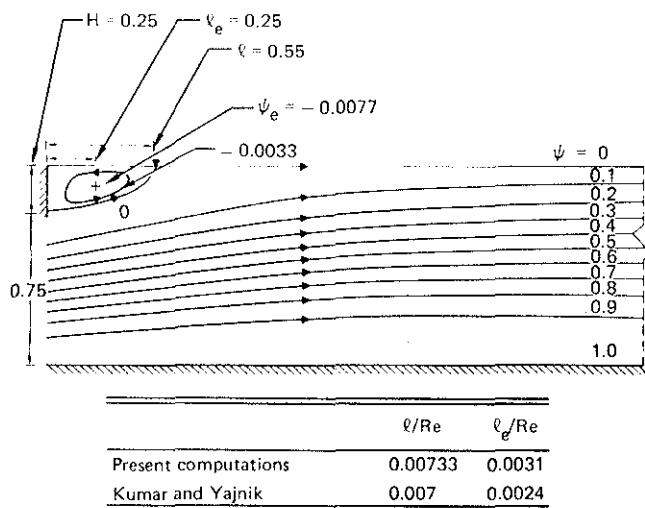


Fig. 24 Streamline- ψ contours for flow in a channel with a blunt base, $Re_H = 18.75$ ($Re = 75$), $H = 0.25$.

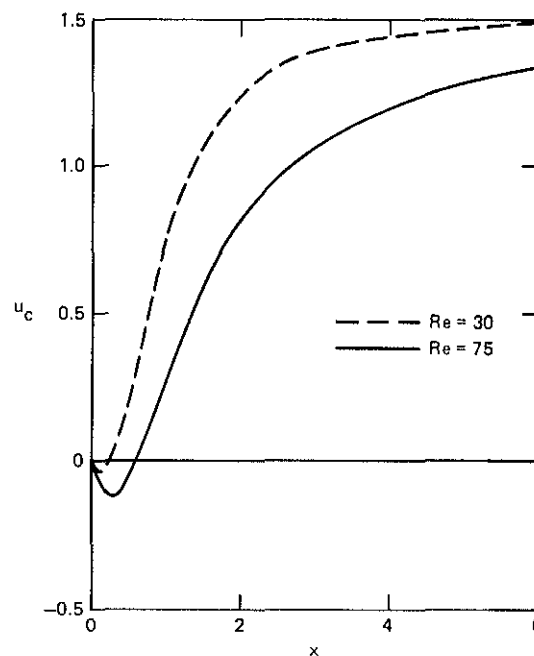


Fig. 25 Centerline velocity distribution for flow in a channel with a base, $H = 0.25$.

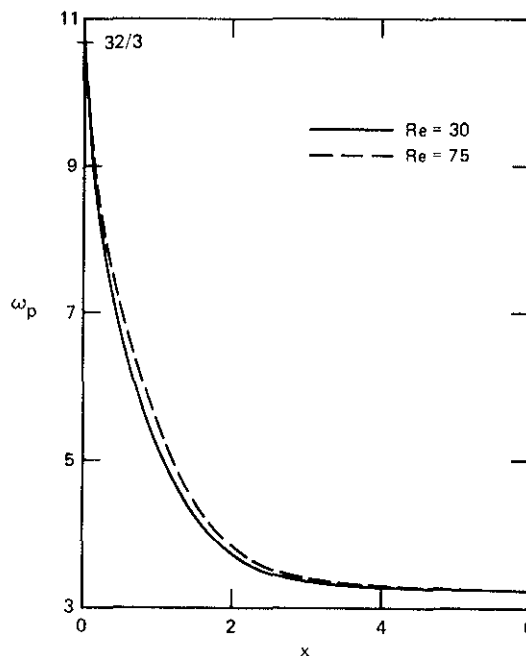


Fig. 26 Distribution of vorticity at the lower wall of the channel with a base, $H = 0.25$.

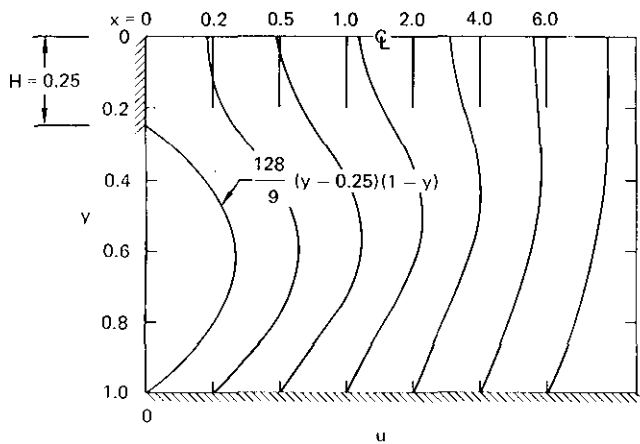


Fig. 27 Streamwise velocity profiles at various streamwise locations (x) for flow in a channel with a base, $Re = 75$, $H = 0.25$.

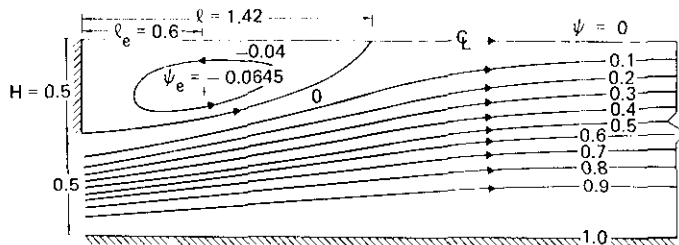


Fig. 28 Streamline- ψ contours for flow in a channel with a blunt base, $Re_H = 25$, ($Re = 50$), $H = 0.5$.

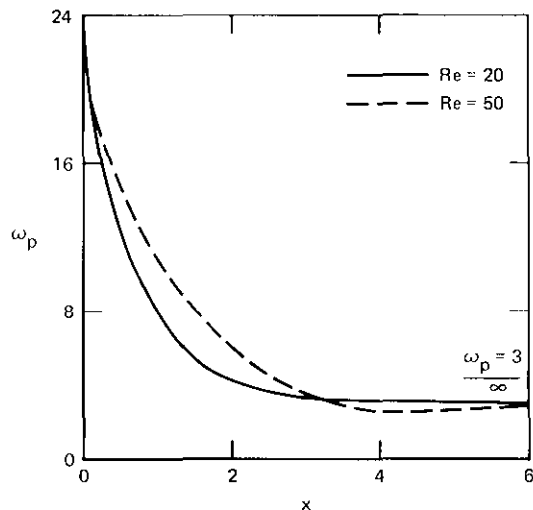


Fig. 29 Distribution of vorticity at the lower wall of the channel with a base, $H = 0.5$.

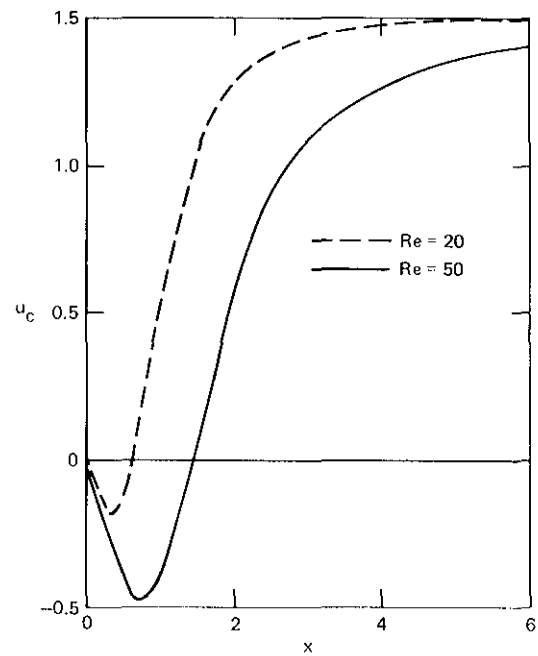


Fig. 30 Centerline velocity distribution for flow in a channel with a base, $H = 0.5$.

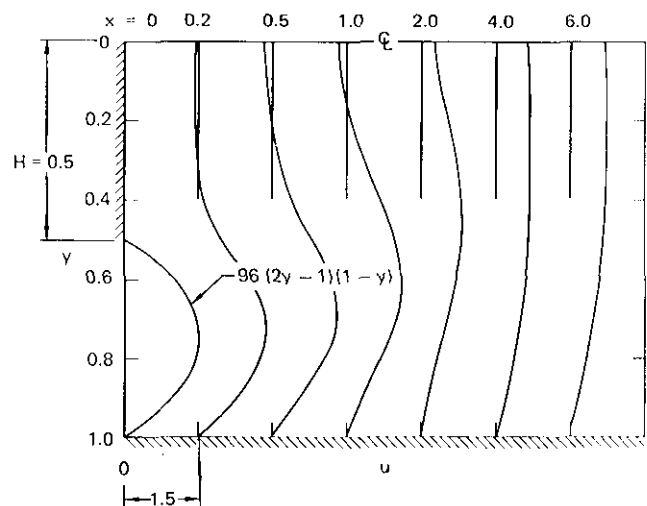


Fig. 31 Streamwise velocity profiles at various streamwise locations (x) for flow in a channel with a base, $Re = 50$, $H = 0.5$.

Flowfield of an Impinging Jet

Figure 32 shows the geometry and boundary conditions for the flowfield of an impinging jet. At the inflow boundary of the computational domain, a self-similar laminar-jet profile is specified. This profile has also been used by Atias, Wolfshtein, and Israeli³ in their study of this flow. The stream function and vorticity at the inflow boundary are given by

$$\psi = -\tanh(6x)/6 \quad (16a)$$

$$\omega = 72\psi(1-36\psi^2). \quad (16b)$$

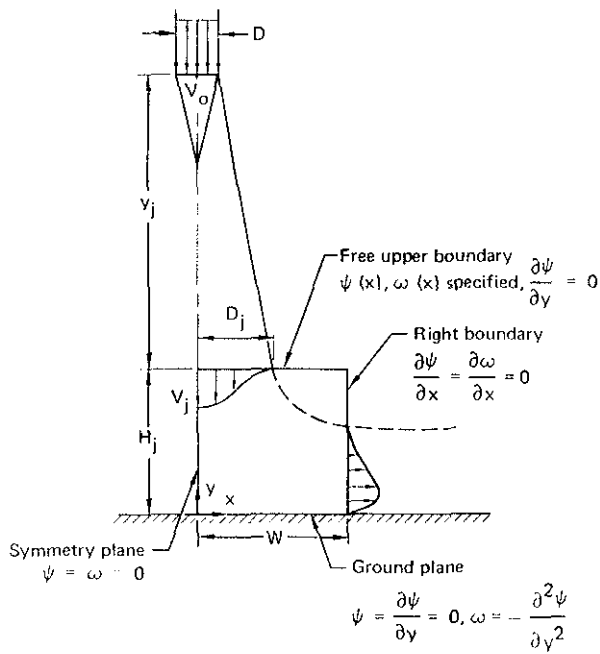


Fig. 32 Definition of the computational region of the planar impinging jet.

The Reynolds number for this flow Re_j is based on the maximum jet velocity at the inflow boundary and the height H_j of the jet above the ground plane. Computations are carried out for $Re_j = 100$ and 250 . The width of the computational domain W is taken to be $2H_j$. The mesh is uniform with spacing $h = 0.05$. The streamline and vorticity contours for this flow are shown in Figs. 33 and 34. ψ -contours show the turning of the jet and the mass-entrainment. The vorticity distribution shows the convection of ω to the right and the development of boundary layers on the ground plane. The detailed comparison for this flow with the computations of other investigators has not been possible because of the unavailability of other results at these laminar Reynolds numbers. Atias, Wolfshtein, and Israeli³ present only one numerical result for this flow, the maximal vorticity at the downstream boundary of the control volume. The present result for this quantity at $Re_j = 100$ is 1.14 which compares well with their result (≈ 1.2) using a central ADI scheme. However, we note that this is not a meaningful quantity to compare the results of various computations. A more meaningful quantity is the value of maximum vorticity (ω_{pmax}) at the ground plane:

Re_j	$(\omega_p)_{max}$
100	4.1
250	7.3

Figure 35 shows the development of a wall-jet type of velocity profile away from the stagnation region. Figure 36 shows the dramatic change in v -velocity distribution at various x locations.

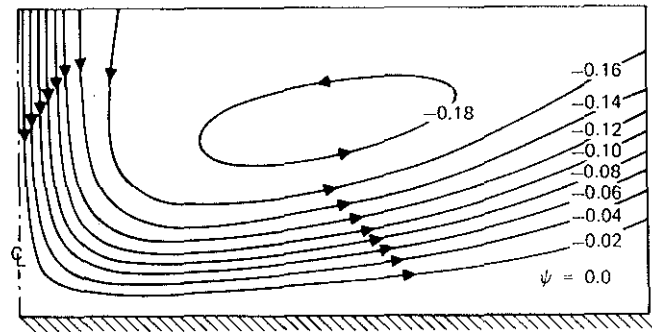


Fig. 33 Streamline- ψ contours for the impinging-jet flow at $Re_j = 2.5 \times 10^2$.

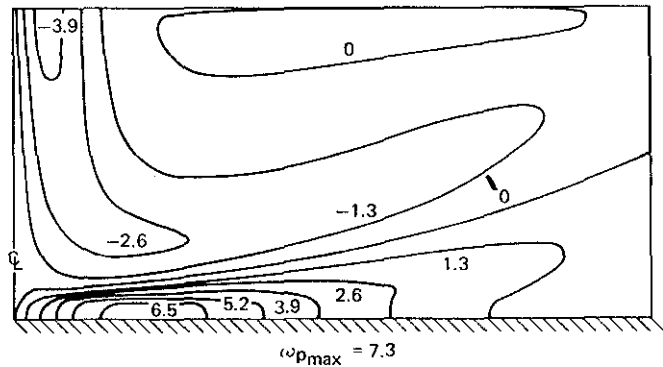


Fig. 34 Vorticity- ω contours for the impinging-jet flow at $Re_j = 2.5 \times 10^2$.

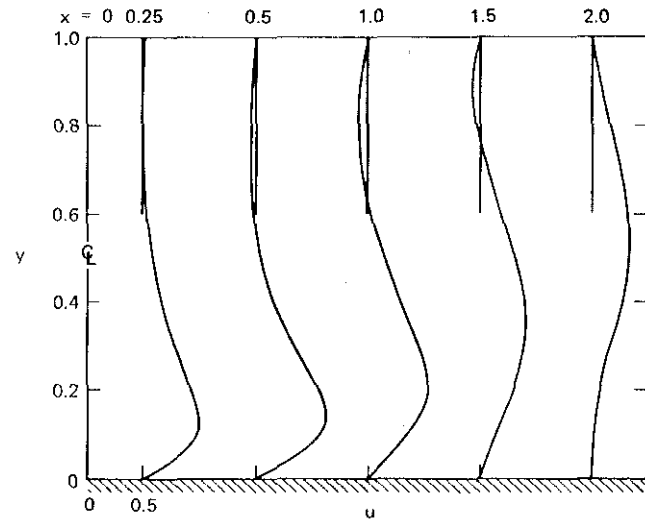


Fig. 35 u -velocity profiles at various x locations for impinging-jet flow at $Re_j = 2.5 \times 10^2$.

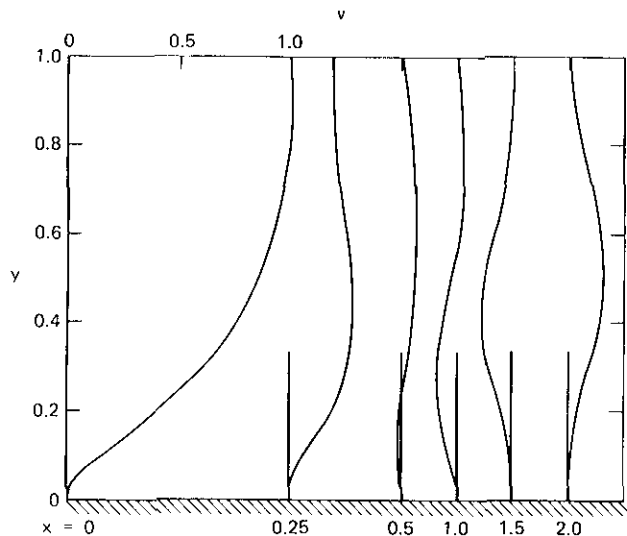


Fig. 36 v-velocity profiles at various x locations for impinging-jet flow at $Re_j = 2.5 \times 10^2$.

Summary

A third-order-accurate upwind scheme has been formulated for the numerical solution of 2-D Navier-Stokes equations in stream-function/vorticity form. Numerical experiments on a variety of flows with large recirculating regions indicate that the scheme is stable and accurate at high Reynolds numbers. Highly accurate solutions for flow in a driven square cavity for Reynolds numbers up to 7.5×10^4 reveal an extraordinary flow-structure never obtained before using the steady Navier-Stokes equations. For other separating and reattaching flows such as flow in a channel with a sudden expansion, flow in a channel with a base, and the impinging jet flow, excellent agreement is obtained with the computation of other investigators as well as with the available experimental data.

References

1. Nallasamy, M. and Prasad, K. K., "Numerical Studies on Quasilinear and Linear Elliptic Equations," *J. Comput. Phys.* **15**, 429-448 (1974).
2. Patankar, S. V. and Spalding, D. B., "A Calculation Procedure for Heat, Mass and Momentum Transfer in Three-Dimensional Parabolic Flows," *Int. J. Heat Mass Transfer* **15**, 1787-1806 (1972).
3. Alias, M., Wolfshtein, M. and Israeli, M., "Efficiency of Navier-Stokes Solvers," *AIAA J.* **15**, 263-266 (1977).
4. Gupta, M. M. and Manohar, R. P., "Boundary Approximations and Accuracy in Viscous Flow Computations," *J. Comput. Phys.* **31**, 265-288 (1979).
5. Bontoux, P., Gilly, B. and Roux, B., "Analysis of the Effect of Boundary Conditions on Numerical Stability of Solutions of Navier-Stokes Equations," *J. Comput. Phys.* **36**, 417-427 (1980).
6. Woods, L. C., "A Note on the Numerical Solution of Fourth-Order Differential Equations," *Aero. Quart.* **5**, 176 (1954).
7. Benjamin, A. S. and Denny, V. E., "On the Convergence of Numerical Solutions for 2-D Flows in Cavity at Large Re," *J. Comput. Phys.* **33**, 340-358 (1979).
8. Leonard, B. P., "A Stable and Accurate Convective Modelling Procedure Based on Quadratic Upstream Interpolation," *Computer Methods in Appl. Mech. and Engg.* **19**, 59-98 (1979).
9. Roache, P. J., *Computational Fluid Dynamics*, (Hermosa Publishers, Albuquerque, NM, 1972).
10. Mueller, T. J. and O'Leary, R. A., "Physical and Numerical Experiments in Laminar Incompressible Separating and Re-attaching Flows," *AIAA Paper No. 70-763* (1970).
11. Hung, T. K. and Macagno, E. O., "Laminar Eddies in a Two-Dimensional Conduit Expansion," *La Houille Blanche* **21**, 391-400 (1966).
12. Burggraf, O. R., "Analytical and Numerical Studies of the Structure of Steady Separated Flow," *J. Fluid. Mech.* **24**, 113-151 (1966).
13. Rubin, S. G. and Khosla, P. K., "Navier-Stokes Calculations with a Coupled Strongly Implicit Method, Part I: Finite Difference Solutions," *AIAA Paper No. 79-0011* (1979).
14. Mallison, G. D. and De Vahl Davis, G., "The Method of the False Transients for the Solution of Coupled Elliptic Equations," *J. Comput. Phys.* **12**, 435-461 (1973).
15. Batchelor, G. K., "On Steady Laminar Flow with Closed Streamlines at Large Reynolds Numbers," *J. Fluid Mech.* **1**, 177-190 (1956).
16. Moffatt, H. K., "Viscous and Resistive Eddies near a Sharp Corner," *J. Fluid Mech.* **18**, 1-18 (1964).
17. Kumar, A. and Yajnik, K. S., "Separated Flows at Large Reynolds Numbers," *J. Fluid Mech.* **97**, 27-51 (1980).
18. Durst, F., Melling, A. and Whitelaw, J. H., "Low Reynolds Number Flow Over a Plane Symmetric Sudden Expansion," *J. Fluid Mech.* **64**, 111-128 (1974).
19. Acrivos, A., Leal, L. G., Snowden, D. D. and Pan, F., "Further Experiments on Steady Flows Past Bluff Objects," *J. Fluid Mech.* **34**, 25-48 (1968).
20. Goldstein, R. J., et al., "Laminar Separation, Reattachment, and Transition of the Flow Over a Downstream Facing Step," *ASME Paper No. 69-WA/FE-5* (1969).